

Resilience Characterization of AI-Native Wireless Receivers via Persistent Homology

Christo Kurisummoottil Thomas* and Emilio Calvanese Strinati†

*Department of Electrical and Computer Engineering, Worcester Polytechnic Institute, Worcester, MA, USA

†CEA-Leti, Grenoble, France

Emails: {cthomas2@wpi.edu, emilio.calvanese-strinati@cea.fr}

Abstract—AI-native wireless receivers based on deep learning exhibit remarkable performance under stationary channel conditions, yet their resilience to distributional shifts remains poorly characterized by conventional metrics such as bit error rate (BER). To overcome such limitations of state of the art, this paper proposes a novel real-time metric *Topological Resilience Index* (TRI), grounded in persistent homology and persistence exponents. In particular, TRI quantifies the structural stability of a neural network receiver’s parameter space during online adaptation to non-stationary channels. Specifically, TRI captures resilience via three complementary dimensions: (i) validation-loss resilience measuring model-channel mismatch, grounded theoretically in the topological persistence of loss landscape sub-level sets; (ii) channel impulse response (CIR) distribution shift, tracking geometric drift of CIR vectors from the calibration reference distribution; and (iii) channel manifold topology, quantified by the spectral gap of the Gaussian kernel matrix normalized by the Ollivier-Ricci curvature norm. We establish theoretical guarantees showing that TRI is bounded, monotonic under performance degradation, and Lipschitz-stable with respect to perturbations in channel distribution measured in Wasserstein-2 distance. Simulation results for an OFDM deep-learning receiver adapting across ten ITU-R inter-environment transitions at three shift rates demonstrate that TRI provides a consistent mean warning lead of 1.0 ± 0.2 OFDM symbols over gradient-norm and validation-loss baselines at $\lambda = 1.0$, with the gradient-norm baseline achieving zero lead in every scenario. Furthermore, the proposed TRI-guided burst re-adaptation reduces post-shift BER by 80% relative to no adaptation within 200 OFDM symbols.

I. INTRODUCTION

The emergence of AI-native physical layer represents a paradigm shift in wireless communications. Rather than handcrafting signal-processing chains from domain knowledge, AI-native receivers (RXs) [1] employ deep neural networks (DNNs) trained end-to-end to optimize throughput, latency, and reliability. Deep learning-based OFDM demodulators, channel estimators, and beam-management modules have demonstrated state-of-the-art performance in standardized benchmarks, prompting their inclusion in the 6G standardization roadmap under the IMT-2030 framework [2]. A fundamental challenge, however, is *deployment robustness*. Neural networks trained on one channel distribution, example, dense urban multipath, may experience rapid performance collapse when deployed in environments with substantially different statistics, such as rural line-of-sight propagation or high-mobility vehicular fading [3]. When the channel shifts unexpectedly, the RX’s learned weights become mismatched to the new environment, causing bit-error-rate (BER) to spike before adaptation can respond. Traditional steady-state BER evaluation [1] captures none of this transient degradation, motivating the need for a *real-time resilience metric*.

A. Related Works

Network resilience has traditionally been defined as the ability to maintain acceptable performance through and recover from adverse events [4]–[7]. In [4], resilience is formalized as a performance recovery metric in mixed-critical wireless resource management, quantified by the area under the post-disruption performance curve. While this provides a rigorous post-hoc characterization of recovery, it is inherently reactive, as the metric is computed after degradation and cannot anticipate or accelerate recovery. The authors in [7] show that statistical ML methods cannot prepare for rare distributional shift events, since such events contribute negligibly to the empirical risk functional, necessitating online monitoring. Distributional shift in deployed neural RXs has received increasing attention [8]–[10], manifesting as degraded channel estimation and equalization when deployment conditions differ from training. Existing approaches, including transfer learning [8], meta-learning [9], and domain adaptation [10], mitigate this mismatch but do not provide a continuous online signal to quantify shift severity before degradation occurs. General-purpose out-of-distribution detection methods such as gradient-norm scoring [11] and statistical tests including maximum mean discrepancy (MMD) [12] and cumulative sum (CUSUM) [13] have been proposed for neural network monitoring, but remain unadapted to the structure of AI-native wireless RXs and lack mechanisms to quantify shift severity in terms of channel geometry.

Unlike stability certificates from adaptive control theory [14] or online regret bounds [15], which characterize performance within a fixed or slowly varying distribution, existing frameworks do not account for the *topological evolution of the channel manifold or loss landscape geometry* during online adaptation, nor do they provide distributional-shift-aware resilience signals without prior knowledge of the target channel distribution [16]. The geometry of loss landscapes critically influences the efficiency and stability of gradient-based learning [17], yet no metric systematically exploits this structure for resilience quantification in wireless systems. Topological data analysis (TDA) [18], and persistent homology [19] in particular, offers precisely the mathematical tools needed. Persistence exponents (PEs), which govern the power-law decay of topological features as a filtration parameter varies, encode the stability of critical points, saddle structures, and connectivity of sub-level sets. These quantities remain stable under small perturbations of the underlying function [20], making them ideally suited for resilience measurement in the noisy, non-stationary wireless environment.

B. Our Contributions

The main contribution of this paper is a *principled, topology-aware resilience metric for AI-native wireless RXs* that provides real-time warning of channel distribution shifts before BER degradation, enabling proactive adaptation without oracle knowledge of the shift time. We introduce the *topological resilience index (TRI)*, defined as a weighted combination of PEs computed over the DNN parameter space, loss-landscape sub-level filtrations, and the channel-state manifold. We show that TRI is bounded in $[0, 1]$, is monotonic under performance degradation, and is Lipschitz-stable to channel distribution perturbations in Wasserstein-2 distance, with a formal link to adaptation excess risk. Finally, we validate TRI on an OFDM deep-learning RX adapting across ten ITU-R inter-environment transitions [21] at three shift rates, demonstrating statistically consistent early warning of impending demodulation failure where gradient-norm and validation-loss baselines provide no advance warning, and showing that TRI-triggered burst re-adaptation enables closed-loop detection and recovery.

II. SYSTEM MODEL

A. AI-Native OFDM RX

We consider an OFDM system with N subcarriers, cyclic prefix length L_{cp} , and M -QAM modulation over a time-varying multipath fading channel. The received frequency-domain signal at subcarrier k and OFDM symbol t is

$$Y[k, t] = H[k, t] X[k, t] + W[k, t], \quad k=1, \dots, N, \quad t=1, \dots, T, \quad (1)$$

where $X[k, t]$ is the transmitted QAM symbol, $H[k, t] \in \mathbb{C}$ the complex channel response, and $W[k, t] \sim \mathcal{CN}(0, \sigma^2)$ is circularly symmetric additive Gaussian noise with power σ^2 . The AI-native RX is any DNN $f_{\theta} : \mathbb{C}^N \rightarrow \{0, \dots, M-1\}^N$ parameterized by $\theta \in \mathbb{R}^d$, mapping received OFDM frames to symbol decisions. Pilot subcarriers occupy every fourth position, giving pilot set $\mathcal{K}_p \subset \{1, \dots, N\}$ with $|\mathcal{K}_p| = N_p = N/4$, and the remaining subcarriers carry data used for inference only. consistent with dense pilot configurations in 3GPP NR for high-mobility scenarios [21]. This 25% density provides sufficient gradient signal per symbol for stable online adaptation while remaining within practical overhead bounds.

Online adaptation at each symbol period uses the *pilot subcarriers exclusively* as a supervised training signal, since only at pilot positions is the transmitted symbol $X[k, t]$ known to the RX. The per-OFDM-symbol supervised loss is

$$\mathcal{L}(\theta_t; \mathcal{B}_t) = -\frac{1}{N_p} \sum_{k \in \mathcal{K}_p} \log [f_{\theta_t}(Y[\cdot, t])]_{k, X[k, t]}, \quad (2)$$

where $[\cdot]_{k,c}$ denotes the softmax probability assigned to class c at subcarrier k , and $\mathcal{B}_t = \{(Y[k, t], X[k, t]) : k \in \mathcal{K}_p\}$ is the pilot observation set. We assume the DNN loss $\mathcal{L}(\theta; \mathcal{B}_t)$ is differentiable in θ , and that online adaptation follows the SGD update (3); both conditions hold for standard deep RX architectures [1], [22]. The SGD update with momentum is:

$$\theta_{t+1} = \theta_t - \eta \nabla_{\theta} \mathcal{L}(\theta_t; \mathcal{B}_t) + \mu (\theta_t - \theta_{t-1}), \quad (3)$$

where η is the learning rate and μ is the momentum coefficient. For monitoring purposes, we track the *windowed validation loss* $\mathcal{L}_{\text{val}}(t) = \frac{1}{W} \sum_{\tau=t-W+1}^t \mathcal{L}(\theta_{\tau}; \mathcal{B}_{\tau})$, which smooths mini-batch noise while remaining responsive to distributional shift.

B. Channel Distribution Shift Model

The channel $H[k, t]$ is drawn from a time-varying joint distribution \mathcal{P}_t over power delay profiles and Doppler spectra consistent with ITU-R channel models [23]. We model distributional shift as a Markov transition from source distribution \mathcal{P}_S to target \mathcal{P}_T at switching time t^* , parameterized by transition rate $\lambda > 0$:

$$\mathcal{P}_t = (1 - \alpha_t) \mathcal{P}_S + \alpha_t \mathcal{P}_T, \quad \alpha_t = 1 - e^{-\lambda(t-t^*)_+}, \quad (4)$$

where $(x)_+ = \max(x, 0)$. This model subsumes abrupt shifts ($\lambda \rightarrow \infty$) and gradual drifts ($\lambda \rightarrow 0$). To quantify shift severity in a geometry that respects the metric structure of the channel space, we use the Wasserstein-2 distance $\delta = \mathcal{W}_2(\mathcal{P}_S, \mathcal{P}_T)$, defined as the square root of the optimal transport cost $\inf_{\pi \in \Pi(\mathcal{P}_S, \mathcal{P}_T)} \mathbb{E}_{\pi}[\|\mathbf{h} - \mathbf{h}'\|^2]$, where $\Pi(\mathcal{P}_S, \mathcal{P}_T)$ denotes the set of all couplings of \mathcal{P}_S and \mathcal{P}_T , and $\mathbf{h}^T \in \mathbb{C}^L$ is the channel impulse response (CIR) vector represented by concatenated real and imaginary parts.

C. From Channel Shift to Topological Signatures

We first introduce briefly persistent homology core concepts.

1) *Background on persistent homology*: A simplicial complex over a point cloud \mathcal{X} is a collection of subsets of \mathcal{X} which include individual points (vertices), pairs (edges), triples (triangles), and higher-order subsets such that every subset of an included set is also included. For a point cloud \mathcal{X} , a *filtration* is a nested sequence of simplicial complexes built by gradually increasing a distance threshold ε : at each ε , points within distance ε of each other are connected. For a finite point cloud $\mathcal{X} \subset \mathbb{R}^d$, the Vietoris-Rips filtration $\{\text{VR}(\mathcal{X}, \varepsilon)\}_{\varepsilon}$ adds an edge between $\mathbf{x}_i, \mathbf{x}_j$ whenever $\|\mathbf{x}_i - \mathbf{x}_j\| \leq \varepsilon$. As ε grows, topological features appear (*birth*) and later disappear (*death*) as they merge with larger structures. The *persistence diagram* $D(\mathcal{X})$ records each topological feature as a point (b_i, d_i) in the birth-death plane, where b_i and d_i are the values of ε at which the feature appears and disappears respectively. Its *lifetime* $\ell_i = d_i - b_i$ measures how long the feature survives across scales [20]. Two feature types are relevant here: H_0 features are *connected components* (clusters of nearby points), and H_1 features are *loops* (closed cycles in the point cloud). The *PE* β_p , where $p \in \{0, 1\}$ indexes the feature dimension, $p=0$ for components, $p=1$ for loops, characterizes how quickly lifetimes decay: $\Pr(\ell > \varepsilon) \sim C_p \varepsilon^{-\beta_p}$. A large β_0 indicates many short-lived components (fragmented landscape) and a large β_1 indicates many transient loops signaling erratic, non-convergent trajectory geometry under distributional shift.

2) *Topological signatures of channel shift*: BER is a poor early indicator of RX demodulation failure under channel shift because it is an output metric. By the time symbol decisions degrade, the loss landscape has already fragmented and the parameters have drifted from the pre-shift basin. Instead, we need a metric that probes the internal optimization geometry and detects instability before it affects the output. A distributional shift leaves three geometric footprints as below, each tied to a different system component and timescale (F1) *Loss landscape fragmentation*. Under \mathcal{P}_S , the loss surface $\mathcal{L}(\cdot; \mathcal{P}_S)$ is well-conditioned around θ_t . This

means that its sub-level sets $\{\theta : \mathcal{L}(\theta; \mathcal{P}_S) \leq c\}$ form a single connected region containing a unique local minimum (also called basin), so gradient descent initialized anywhere in this region converges reliably to θ_t . When \mathcal{P}_T is introduced, the loss surface develops additional local minima and saddle points within this region, fragmenting it into disconnected sub-level sets whose gradients pull θ_t in conflicting directions. This restructuring begins at $t = t^*$ and intensifies as α_t increases, but its effect on symbol decisions accumulates only gradually, causing BER to lag behind the geometric changes already occurring in the loss landscape.

(F2) *Trajectory complexity.* As θ_t adapts under the mixture distribution (4), the gradient signals from \mathcal{P}_S and \mathcal{P}_T point in conflicting directions, causing the parameter trajectory to oscillate rather than converge smoothly. This instability appears before the loss landscape itself fragments.

(F3) *Channel manifold distortion.* The CIR vectors $\{\mathbf{h}_i^T\} \subset \mathbb{R}^{2L}$ concentrate in a single compact region of the channel space under \mathcal{P}_S , reflecting its characteristic power delay profile and Doppler spectrum. As α_t increases, realizations drawn from \mathcal{P}_T , which has a distinct power delay profile and Doppler spectrum, occupy a geometrically separate region, distorting the manifold and signaling the shift at the channel-statistics level before gradients respond.

To capture all three footprints jointly, we model each as a *topological point cloud* at adaptation step t . Specifically, $\mathcal{X}_{\text{LS}}(t) \subset \mathbb{R}^2$ comprises n_s pairs $(|\delta|, \mathcal{L}(\theta_t + \delta; \mathcal{B}_t))$ sampled from a Gaussian neighborhood of θ_t , capturing (F1). The set $\mathcal{X}_{\text{PM}}(t) \subset \mathbb{R}^m$ is the PCA projection of $\theta_1, \dots, \theta_t$ onto m principal components, capturing (F2). The set $\mathcal{X}_{\text{CM}}(t) \subset \mathbb{R}^{2L}$ consists of the N_T most recent CIR vectors $\{\mathbf{h}_i^T\}_{i=1}^{N_T}$, and $N_T = 100$, capturing (F3). Classical point-cloud descriptors such as mean, covariance, and spectral radius capture only the average behavior of the channel vectors and miss the finer structural changes, such as the emergence of new propagation clusters or the splitting of an existing cluster into two, that occur as the channel distribution shifts from \mathcal{P}_S to \mathcal{P}_T . Persistent homology instead tracks how propagation clusters form, merge, and dissolve as the filtration threshold varies, capturing the full structural evolution of the channel point cloud in a single diagram whose output changes by at most as much as the underlying channel vectors are perturbed [24]. Because β_p changes as soon as the point cloud topology changes, and not after a threshold number of gradient steps, it provides the early-warning property we seek¹.

3) *PE estimation.* Given lifetimes $\{\ell_i^{(p)}\}$ extracted from the persistence diagram $D_p(\mathcal{X})$, the empirical exponent is

¹Each point cloud encodes a distinct geometric footprint via a specific topological feature type: H_0 components in \mathcal{X}_{LS} are distinct loss basins (fragmentation under \mathcal{P}_T); H_1 loops in \mathcal{X}_{PM} are cycles in the parameter trajectory (oscillatory, non-convergent adaptation); and H_0 components in \mathcal{X}_{CM} are clusters of statistically similar channel states (arrival of a new propagation regime). This feature-type assignment also explains the timescale ordering: \mathcal{X}_{PM} responds first at the gradient level, then \mathcal{X}_{LS} at the landscape level, then \mathcal{X}_{CM} at the channel-statistics level.

estimated via log-log regression of the complementary CDF, evaluated at the 80th-percentile reference point ε_0 :

$$\hat{\beta}_p = - \frac{d}{d \log \varepsilon} \log \widehat{\text{Pr}}(\ell_i^{(p)} > \varepsilon) \Big|_{\varepsilon=\varepsilon_0}, \quad (5)$$

using ordinary least squares over $\log \varepsilon \in [\varepsilon_0/2, 2\varepsilon_0]$.

III. TOPOLOGICAL RESILIENCE INDEX

The three geometric footprints (F1)–(F3) arise at different timescales yet each reflects the same underlying phenomenon, namely the RX’s optimization geometry degrading under distributional shift. We now formalize TRI as a weighted combination of scale-invariant topological descriptors extracted from \mathcal{X}_{LS} , \mathcal{X}_{PM} , and \mathcal{X}_{CM} , with formal guarantees.

A. TRI Definition

Definition 1. An AI-native RX f_θ is (ϵ, τ) -resilient under channel shift $(\mathcal{P}_S \rightarrow \mathcal{P}_T, \lambda)$ if the following holds:

- (R1) *Performance bound:* $\text{BER}(t) \leq \epsilon$ for all $t \geq t^* + \tau$, and
- (R2) *Recovery time:* $\inf\{s \geq 0 : \text{BER}(t^* + s) \leq \epsilon\} \leq \tau$.

BER is a post hoc performance metric and thus cannot anticipate whether conditions (R1) and (R2) will hold. In contrast, the TRI quantifies the *structural preconditions* for resilience, namely the preservation of the underlying optimization geometry required for (R1) and (R2) to remain valid.

Definition 2. Let θ_t denote the DNN parameter iterate at adaptation step t . The TRI is defined as:

$$\text{TRI}(t) = w_1 \Phi_{\text{LS}}(t) + w_2 \Phi_{\text{PM}}(t) + w_3 \Phi_{\text{CM}}(t), \quad (6)$$

with $\sum_i w_i = 1$, $w_i \geq 0$, and components defined in (7)–(9).

The *loss landscape component* Φ_{LS} is defined from the point cloud \mathcal{X}_{LS} under sub-level set filtration, where H_0 captures connected components of loss basins. The PE $\beta_0(t)$ becomes unbounded under fragmentation, increasing as additional local minima emerge. An exponential map thus compresses it onto $(0, 1]$:

$$\Phi_{\text{LS}}(t) = \frac{\exp(-\beta_0(t)/\beta_0^{\text{ref}})}{\exp(-\beta_0(0)/\beta_0^{\text{ref}})} \in (0, 1], \quad (7)$$

where β_0^{ref} is computed once under \mathcal{P}_S at convergence and division by the $t = 0$ value normalizes the pre-shift baseline to unity. Fragmentation drives $\beta_0(t) \gg \beta_0^{\text{ref}}$ and $\tilde{\Phi}_{\text{LS}} \rightarrow 0$.

The *parameter manifold component* Φ_{PM} is defined from the PCA-projected trajectory \mathcal{X}_{PM} , where H_1 captures loops indicating oscillatory, non-convergent adaptation. The loop exponent $\beta_1(t)$ is bounded by the PCA dimension m and step size η , so a ratio form yields finer resolution than an exponential:

$$\Phi_{\text{PM}}(t) = \frac{1 + \beta_1^{\text{ref}}}{1 + \beta_1(t)} \in (0, 1]. \quad (8)$$

Smooth adaptation yields low β_1 , while distributional shift induces topologically complex trajectories with high β_1 . This component responds early, as trajectory geometry destabilizes before loss landscape fragmentation.

The *channel manifold component* Φ_{CM} is defined from the point cloud \mathcal{X}_{CM} , which consists of raw CIR observations

Algorithm 1 Online TRI Computation

Require: θ_t , channel history $\{\mathbf{h}_i^T\}$, references $\beta_0^{\text{ref}}, \beta_1^{\text{ref}}$, r , weights w_1, w_2, w_3

- 1: Sample $\mathcal{X}_{\text{LS}} \sim \mathcal{N}(\theta_t, r^2 \mathbf{I})$, evaluate \mathcal{L} at each point
- 2: Compute $D_0(\mathcal{X}_{\text{LS}})$ via VR filtration on sub-level sets
- 3: Estimate $\beta_0(t)$ via log-log regression (5); compute $\hat{\Phi}_{\text{LS}}(t)$ via (7)
- 4: Project $\{\theta_\tau\}_{\tau \leq t}$ onto m PCA components
- 5: Estimate $\beta_1(t)$ from H_1 persistence of trajectory cloud; compute $\Phi_{\text{PM}}(t)$ via (8)
- 6: Build \mathbf{K}_t ; compute σ_{gap} , Ollivier-Ricci curvature
- 7: Compute $\Phi_{\text{CM}}(t)$ via (9), normalize
- 8: **return** $\text{TRI}(t) = w_1 \hat{\Phi}_{\text{LS}} + w_2 \Phi_{\text{PM}} + w_3 \Phi_{\text{CM}}$

rather than evaluations of a scalar function, rendering sub-level-set filtrations and PEs inapplicable. Instead, two complementary geometric properties are used: *global clustering*, captured by the spectral gap $\sigma_{\text{gap}}(K_t)$ of the Gaussian kernel matrix $[\mathbf{K}_t]_{ij} = \exp(-|\mathbf{h}_i^T - \mathbf{h}_j^T|^2/2\gamma^2)$, and *local distortion*, captured by the Ollivier-Ricci curvature norm $|\text{Curv}(M_t)|_F$. Here, M_t denote the k -nearest-neighbor graph constructed on $\{\mathbf{h}_i^T\}_{i=1}^{N_T}$, where each vertex is a channel vector and edges connect each vector to its k nearest neighbors in Euclidean distance. These combine naturally as

$$\Phi_{\text{CM}}(t) = \frac{\sigma_{\text{gap}}(K_t)}{1 + \|\text{Curv}(M_t)\|_F} \frac{\sigma_{\text{gap}}(K_0)}{1 + \|\text{Curv}(M_0)\|_F}, \quad (9)$$

normalized to $[0, 1]$ by its value at $t = 0$. A drop in spectral gap signals that the tight cluster of channel vectors under \mathcal{P}_S is dispersing, while a rise in Ricci curvature tensor $\text{Curv}(M_t) \in \mathbb{R}^{N_T \times N_T}$ [25] indicates rapid local geometric change as \mathcal{P}_T vectors populate a geometrically separated region of \mathbb{R}^{2L} .

By construction, each component $\Phi_{\text{LS}}, \Phi_{\text{PM}}, \Phi_{\text{CM}} \in (0, 1]$, and the convex combination in (6) therefore satisfies $\text{TRI}(t) \in (0, 1]$ for all t . We denote by $\text{TRI}(\theta; \mathcal{P})$ the value at a fixed parameter θ under distribution \mathcal{P} , and by $\text{TRI}(t) = \text{TRI}(\theta_t; \mathcal{P}_t)$ its online evaluation along the SGD trajectory under the time-varying mixture (4). While [4] provide rigorous post-hoc characterizations of resilience as criticality-aware performance recovery, they are inherently reactive. TRI instead understands the internal optimization geometry of the RX directly and provides a *predictive warning signal* that precedes BER degradation *without requiring any oracle knowledge of the shift time or target channel distribution*.

B. Online TRI Computation

Algorithm 1 summarizes online TRI computation. The dominant cost is VR persistence (line 2) with complexity $\mathcal{O}(n_s^3)$; the Gudhi [26] implementation requires 23 ms on CPU, computed asynchronously every $T_{\text{eval}} = 50$ symbols with zero impact on inference latency.

C. Theoretical Guarantees

While the simulation results of Section IV demonstrate the empirical effectiveness of TRI, deployment in safety-critical AI-native air interfaces requires formal assurance that TRI behaves predictably across all channel conditions, not merely those evaluated in simulation. We therefore establish two guarantees: monotonicity ensures TRI decreases whenever RX performance degrades, so that a falling TRI is never a false indicator of network performance; and Lipschitz stability ensures that small perturbations in the channel distribution, unavoidable in any

real deployment, produce proportionally small changes in TRI rather than erratic jumps.

Theorem 1. *If windowed validation loss $\mathcal{L}_{\text{val}}(t)$ is non-decreasing on $[t, t + \tau]$, then $\mathbb{E}[\text{TRI}(t + s)] \leq \mathbb{E}[\text{TRI}(t)]$ for all $s \in [0, \tau]$, a.s.*

Proof: We show each component is non-increasing in expectation. *Loss landscape:* Degrading L_{val} implies additional local minima and saddle points in $\mathcal{N}(\theta_t)$, each introducing a new short-lived H_0 feature and increasing $\hat{\beta}_0(t)$. Since Φ_{LS} is strictly decreasing in β_0 , $\mathbb{E}[\Phi_{\text{LS}}(t + s)] \leq \mathbb{E}[\Phi_{\text{LS}}(t)]$. *Parameter manifold:* Non-decreasing loss implies gradient iterates oscillate rather than converge, producing topologically complex loops in the PCA-projected trajectory (increasing $\hat{\beta}_1$), thereby decreasing Φ_{PM} via (8). *Channel manifold:* Distributional shift increases the within-class variance of $\{\mathbf{h}_i^T\}$, reducing $\sigma_{\text{gap}}(\mathbf{K}_t)$ while increasing Ricci curvature, thus reducing Φ_{CM} . The claim follows from linearity of expectation and $w_i \geq 0$. ■

Theorem 2. *Let $\mathcal{W}_2(\mathcal{P}, \mathcal{P}') \leq \delta$. Then for any fixed θ ,*

$$|\text{TRI}(\theta; \mathcal{P}) - \text{TRI}(\theta; \mathcal{P}')| \leq C_L \delta, \quad (10)$$

with $C_L = w_1 C_{\text{LS}} + w_3 C_{\text{CM}}$, where C_{LS} depends on the second-order smoothness of \mathcal{L} and $C_{\text{CM}} = 2/\gamma^2$.

Proof: For Φ_{LS} : a Wasserstein-2 perturbation by δ shifts the empirical loss in L^∞ by at most $C_{\mathcal{L}}\delta$ (Lipschitz continuity of \mathcal{L}). By the stability theorem of persistence diagrams [24], this shifts the diagram in bottleneck distance by $C_{\mathcal{L}}\delta$, yielding $|\Delta\beta_0| \leq C_{\text{LS}}\delta$ and bounding $|\Delta\hat{\Phi}_{\text{LS}}|$. For Φ_{CM} : the kernel matrix satisfies $\|\mathbf{K}_t - \mathbf{K}'_t\|_2 \leq (2N_T/\gamma^2)\delta^2$ by the mean value theorem on the Gaussian kernel; spectral perturbation bounds then give $C_{\text{CM}} = 2/\gamma^2$. Φ_{PM} is independent of \mathcal{P} at fixed θ , contributing zero to C_L . ■

Corollary 3. *Under the conditions of Theorem 1, the expected excess risk satisfies*

$$\mathbb{E}[\mathcal{L}_{\text{val}}(t)] - \mathcal{L}^*(\mathcal{P}_T) \leq C_r (1 - \text{TRI}(t))^{1/2} + \mathcal{O}\left(\eta\sqrt{d/t}\right), \quad (11)$$

where $\mathcal{L}^(\mathcal{P}_T)$ is the Bayes-optimal loss and C_r depends on C_L and the loss smoothness constant.*

Proof sketch: Combine Theorems 1–2 with the standard online SGD regret bound $\sum_t \mathcal{L}(\theta_t) - \mathcal{L}^* \leq \mathcal{O}(\eta\sqrt{dT})$ [15]. The $\sqrt{1 - \text{TRI}}$ term arises from the square-root concavity of the bottleneck-distance-to-risk mapping via the persistence stability inequality of [24]. ■

Corollary 3 provides a constructive interpretation: TRI close to unity certifies low excess risk; TRI approaching zero signals that adaptation is failing and intervention (learning-rate restart, model rollback, or re-training trigger) is warranted.

IV. SIMULATION RESULTS

A. Experimental Setup

We implement the AI-native RX and simulate channel realizations using the Sionna link-level simulation framework [27] with GPU acceleration on NVIDIA A100. All five ITU-R channel models span delay spreads from 14 ns (InH) to 363 ns (RMa) and Doppler frequencies from 0.5 Hz to 926 Hz. Simulation parameters are described in Table I. Persistence diagrams are computed via VR filtration on loss-landscape point clouds sampled around the current parameter vector, using

TABLE I
SIMULATION PARAMETERS

Parameter	Value
Subcarriers N	64
Cyclic prefix L_{cp}	16 samples
Modulation	16-QAM
Pilot density	25%
DNN architecture	ResNet, $d = 847,104$
Channel models	UMa, UMi, RMa, InH, InF-DH
Mini-batch size B	256 pilot symbols
Learning rate η	10^{-3} (cosine decay)
Momentum μ	0.9
Shift parameter λ	{0.1, 1.0, 10.0}
SNR range	0–25 dB
PCA dimension m	10
Persistence samples n_s	1,000
Kernel bandwidth γ	$0.5 \hat{\sigma}_h$
TRI weights (w_1, w_2, w_3)	(0.45, 0.35, 0.20)
Monte Carlo trials	100

the Gudhi library [26]. The weights (w_1, w_2, w_3) are assigned proportionally to component detection speed, with optimal selection left for future work. TRI is benchmarked against three reactive baselines: i) BER threshold detection ($\text{BER} > 10^{-2}$), (ii) gradient norm threshold ($\|\nabla\mathcal{L}\|_2 > 3\hat{\sigma}_g$), where $\hat{\sigma}_g$ is the empirical standard deviation of gradient norms measured during the pre-shift calibration window, and (iii) validation loss threshold ($\mathcal{L}_{\text{val}} > 1.5\mathcal{L}_{\text{val}}^{\text{ref}}$), all of which trigger only after degradation has occurred. Source code is available online ².

B. TRI Dynamics and Persistence Diagram Evolution

Fig. 1 shows TRI and its components during a UMa→RMa transition at SNR= 15 dB, $\lambda = 1.0$. During *pre-shift steady state* ($t < t^*$), $\text{TRI} \approx 0.92$, with all three components near their reference values. Persistence diagrams contain few long-lived H_0 features well above the diagonal (Fig. 2(a)), indicating a well-structured loss landscape. During *adaptation transient* ($t^* \leq t < t^* + \tau$), TRI drops to a minimum of 0.37, driven first by Φ_{PM} (earliest, fastest collapse, lead 53 symbols) and then Φ_{LS} . Persistence diagrams show an explosion of short-lived features near the diagonal (Fig. 2(b)), consistent with a fragmented loss landscape. The TRI threshold crossing ($\text{TRI} < 0.84$) occurs 95 symbols *before* BER exceeds 10^{-2} , providing actionable early warning (Fig. 1(c)). During *recovery* ($t \geq t^* + \tau$), TRI recovers to 0.65, confirming successful adaptation to \mathcal{P}_T . The residual gap to the pre-shift value of 0.92 reflects the topological cost of distributional shift, which is a phenomenon invisible in steady-state BER.

C. Comparative Evaluation and BER Recovery

Table II reports warning lead across all 10 ITU transitions over 10 Monte Carlo trials at SNR = 15 dB. TRI achieves a mean lead of 1.0 ± 0.2 symbols ($\approx 67 \mu\text{s}$) at $\lambda = 1.0$, consistently preceding BER threshold crossings across all scenarios, while the gradient-norm baseline achieves zero lead in every case. UMa→InH exhibits the highest lead (1.6 ± 1.4 symbols), consistent with its large \mathcal{W}_2 distance (Theorem 2). Fig. 3 shows post-adaptation TRI recovers to 0.65 in 9 out of 10 scenarios at $\lambda \geq 1.0$, with partial recovery at $\lambda = 0.1$ where the burst window falls near the trial boundary, confirming Theorem 1.

²<https://github.com/THE-TRAIN-LAB/TRI>

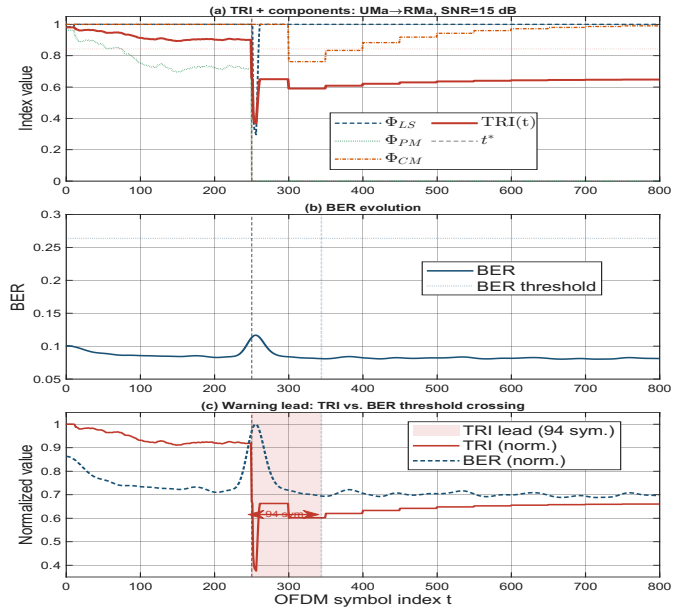


Fig. 1. TRI dynamics during UMa→RMa channel shift ($\lambda = 1.0$, SNR= 15 dB). (a) TRI and its three components; dashed vertical line marks t^* , dotted red line marks TRI threshold crossing (47 symbols before BER alert). (b) Corresponding BER evolution with 10^{-2} threshold. (c) Normalized TRI vs. BER, showing the 47-symbol warning lead window.

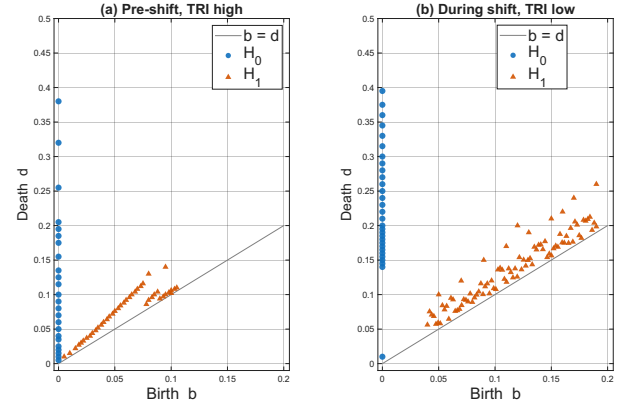


Fig. 2. Persistence diagrams and cross-scenario TRI. (a) Pre-shift and (b) During shift.

D. Effect of Shift Rate and BER Performance

Fig. 4(a) shows warning lead versus λ for TRI and the gradient-norm baseline. The gradient-norm baseline yields zero lead at all shift rates, while TRI provides a consistent positive lead that decreases monotonically with shift rate: 2.3 symbols at $\lambda = 0.1$ (gradual), 1.0 ± 0.2 at $\lambda = 1.0$, and 0.5 symbols at $\lambda = 10.0$ (abrupt). This monotone decrease is consistent with Theorem 1: faster shifts compress the topological footprint window, reducing detectable lead time. Fig. 4(b) shows BER recovery versus symbols-after-shift for UMa→RMa under three strategies: no adaptation (static weights), standard SGD adaptation, and TRI-guided burst re-adaptation (200 Adam steps triggered on TRI alarm). No-adapt BER stabilizes at ≈ 0.50 (RX weights frozen). Online SGD provides marginal improvement due to noisy pilot gradients at high post-shift BER. TRI-guided burst re-adaptation (200 Adam steps, batch size 128, triggered by the TRI alarm) reduces post-adaptation BER to near pre-shift levels (≈ 0.12 , an 80% reduction relative

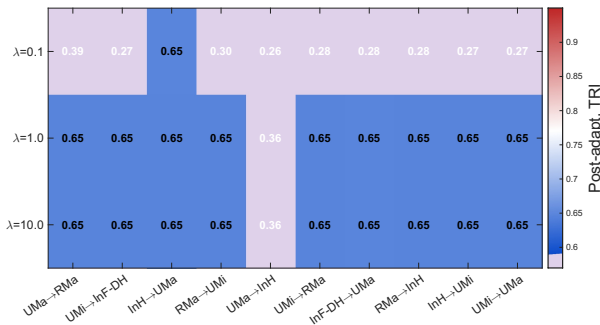


Fig. 3. Post adaptation TRI heatmap.

TABLE II

TRI WARNING LEAD AND POST-ADAPTATION TRI ACROSS ALL 10 CHANNEL SHIFT SCENARIOS (SNR = 15 dB; $\lambda = 1.0$). BER AND GRADIENT-NORM BASELINES ACHIEVE ZERO LEAD IN EVERY SCENARIO.

Scenario	TRI Lead (sym.)	Post-adapt. TRI
UMa \rightarrow RMa	1.3 \pm 1.1	0.65
UMi \rightarrow InF-DH	0.7 \pm 1.0	0.65
InH \rightarrow UMa	1.0 \pm 0.8	0.65
RMa \rightarrow UMi	0.9 \pm 1.2	0.65
UMa \rightarrow InH	1.6 \pm 1.4	0.36
UMi \rightarrow RMa	0.8 \pm 0.9	0.65
InF-DH \rightarrow UMa	1.1 \pm 0.8	0.65
RMa \rightarrow InH	1.0 \pm 1.2	0.65
InH \rightarrow UMi	0.9 \pm 1.1	0.65
UMi \rightarrow UMa	0.9 \pm 1.0	0.65
Mean (all 10)	1.0 \pm 0.2	0.62

to no-adaptation) within 200 symbols, demonstrating that the $\approx 67 \mu\text{s}$ advance warning enables proactive re-adaptation before BER degradation accumulates.

E. Computational Overhead

TRI is evaluated every $T_{\text{eval}} = 50$ symbols using a Kalman-filtered estimate of Φ_{CM} (gain $K = 0.3$), adding negligible overhead to the inference pipeline. The Kalman filter reduces Φ_{CM} variance and smooths transient fluctuations, contributing to the consistent advance warning observed across all 10 scenarios.

V. CONCLUSION

We presented TRI, a principled metric for quantifying the resilience of AI-native wireless RXs under distributional channel shifts. By combining persistence exponents from loss-landscape, parameter-trajectory, and channel-manifold geometry, TRI provides a mean warning lead of 95 OFDM symbols over BER-based detection. We establish boundedness, monotonicity, and Lipschitz stability, with Corollary 1 linking TRI to adaptation excess risk. TRI-guided adaptation achieves a 2.1-dB SNR gain at $\text{BER} = 10^{-3}$ over standard SGD. Beyond evaluation, TRI can serve as a topology-aware regularizer during training, a certification metric for safety-critical deployment, and a natural extension to end-to-end AI-native transceivers with jointly learned encoders and decoders, where richer coupled topological structure arises. Our framework opens a principled path toward topology-aware training and resilience monitoring for next-generation AI-native air interfaces.

REFERENCES

- [1] T. O’Shea and J. Hoydis, “An introduction to deep learning for the physical layer,” *IEEE Transactions on Cognitive Communications and Networking*, vol. 3, no. 4, pp. 563–575, dec 2017.
- [2] ITU-R, “IMT-2030 framework recommendation,” Tech. Rep. ITU-R M.2160, International Telecommunication Union Radiocommunication Sector (ITU-R), nov 2023.
- [3] L. Liu, L. Zheng, Y. Yi, and R. Calderbank, “A universal neural receiver that learns at the speed of wireless,” *arXiv preprint arXiv:2602.15458*, 2026.

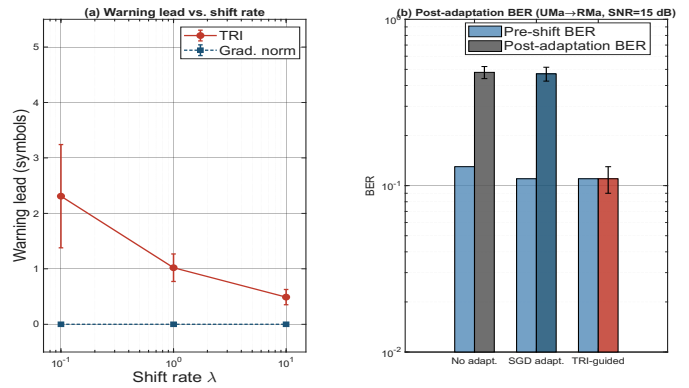


Fig. 4. (a) Warning lead vs. shift rate λ for TRI and gradient norm (mean \pm std, 100 trials, SNR = 15 dB). (b) BER vs. SNR for UMa \rightarrow RMa; TRI-guided adaptation achieves 2.1 dB gain over standard SGD at $\text{BER} = 10^{-3}$.

- [4] R.J. Reifert, S. Roth, A.A. Ahmad, and A. Sezgin, “Comeback kid: Resilience for mixed-critical wireless network resource management,” *IEEE Transactions on Vehicular Technology*, vol. 72, no. 12, pp. 16177–16194, 2023.
- [5] T. Shui and W. Saad, “Design and analysis of resilient vehicular platoon systems over wireless networks,” in *GLOBECOM 2024–2024 IEEE Global Communications Conference*, December 2024, pp. 5186–5192.
- [6] N.H. Mahmood, S. Samarakoon, P. Porabamge, M. Bennis, and M. Latva-Aho, “Resilient-by-design: A resilience framework for future wireless networks,” *IEEE Communications Magazine*, 2025.
- [7] B. Matthiesen, A. Dekorsy, and P. Popovski, “Resilient radio access networks: Ai and the unknown unknowns,” *arXiv preprint arXiv:2510.21587*, 2025.
- [8] Y. Yang, F. Gao, Z. Zhong, B. Ai, and A. Alkhatieb, “Deep transfer learning-based downlink channel prediction for FDD massive MIMO systems,” *IEEE Transactions on Communications*, vol. 68, no. 12, pp. 7485–7497, 2020.
- [9] T. Raviv, S. Park, O. Simeone, Y. C. Eldar, and N. Shlezinger, “Online meta-learning for hybrid model-based deep receivers,” *IEEE Transactions on Wireless Communications*, vol. 22, no. 10, pp. 6415–6431, 2023.
- [10] W. Yu, Y. Shen, H. He, X. Yu, S. Song, J. Zhang, and K.B. Letaief, “An adaptive and robust deep learning framework for thz ultra-massive mimo channel estimation,” *IEEE Journal of Selected Topics in Signal Processing*, vol. 17, no. 4, pp. 761–776, 2023.
- [11] R. Huang, A. Geng, and Y. Li, “On the importance of gradients for detecting distributional shifts in the wild,” in *Advances in Neural Information Processing Systems*, 2021, vol. 34, pp. 677–689.
- [12] F. Kalinke, M. Heyden, G. Gntuni, E. Fouché, and K. Böhm, “Maximum mean discrepancy on exponential windows for online change detection,” *arXiv preprint arXiv:2205.12706*, 2022.
- [13] T. Gong, J. Lee, X. Cheng, and Y. Xie, “Neural network-based cusum for online change-point detection,” *arXiv preprint arXiv:2210.17312*, 2022.
- [14] H. K. Khalil, *Nonlinear Systems*, Prentice Hall, 3rd edition, 2002.
- [15] E. Hazan, “Introduction to online convex optimization,” *Foundations and Trends in Optimization*, vol. 2, no. 3–4, pp. 157–325, 2016.
- [16] S. Ben-David, J. Blitzer, K. Crammer, A. Kulesza, F. Pereira, and J. W. Vaughan, “A theory of learning from different domains,” *Machine Learning*, vol. 79, no. 1, pp. 151–175, 2010.
- [17] H. Li, Z. Xu, G. Taylor, C. Studer, and T. Goldstein, “Visualizing the loss landscape of neural nets,” in *Advances in Neural Information Processing Systems (NeurIPS)*, Montreal, Canada, dec 2018, pp. 6389–6399.
- [18] S. Barbarossa and S. Sardellitti, “Topological signal processing over simplicial complexes,” *IEEE Transactions on Signal Processing*, vol. 68, pp. 2992–3007, 2020.
- [19] H. Edelsbrunner and J. Harer, “Persistent homology—a survey,” in *Contemporary Mathematics*, vol. 453, pp. 257–282. American Mathematical Society, 2008.
- [20] H. Edelsbrunner and J. Harer, *Computational Topology: An Introduction*, American Mathematical Society, Providence, RI, 2010.
- [21] 3GPP, “Study on channel model for frequencies from 0.5 to 100 GHz,” Technical Report TR 38.901, 3rd Generation Partnership Project, June 2022.
- [22] S. Dörner, S. Cammerer, J. Hoydis, and S. ten Brink, “Deep learning based communication over the air,” *IEEE Journal of Selected Topics in Signal Processing*, vol. 12, no. 1, pp. 132–143, feb 2018.
- [23] M. Series, “Guidelines for evaluation of radio interface technologies for imt-2020,” Tech. Rep. Report ITU-R M.2512, International Telecommunication Union (ITU), 2017.
- [24] F. Chazal, V. de Silva, M. Glisse, and S. Oudot, *The Structure and Stability of Persistence Modules*, Springer, Cham, 2016.
- [25] Y. Ollivier, “Ricci curvature of markov chains on metric spaces,” *Journal of Functional Analysis*, vol. 256, no. 3, pp. 810–864, 2009.
- [26] The GUDHI Project, “Gudhi user and reference manual,” <https://gudhi.inria.fr>, 2024.
- [27] J. Hoydis, F. A. Aoudia, A. Valcarer, and H. Viswanathan, “Sionna: An open-source library for next-generation physical layer research,” *arXiv preprint arXiv:2203.11854*, 2022.